

# Oblique drop impact onto a deep liquid pool

Marise V. Gielen,<sup>1,\*</sup> Pascal Sleutel,<sup>1,†</sup> Jos Benschop,<sup>2</sup> Michel Riepen,<sup>2</sup> Victoria Voronina,<sup>2</sup>  
Detlef Lohse,<sup>1</sup> Jacco H. Snoeijer,<sup>1,3</sup> Michel Versluis,<sup>1</sup> and Hanneke Gelderblom<sup>1,‡</sup>

<sup>1</sup>*Physics of Fluids Group, Faculty of Science and Technology,  
MESA+ Institute for Nanotechnology, University of Twente,  
P.O. Box 217, 7500 AE Enschede, The Netherlands.*

<sup>2</sup>*ASML The Netherlands B.V., De Run 6501, 5504 DR Veldhoven, The Netherlands*

<sup>3</sup>*Mesoscopic Transport Phenomena, Eindhoven University of Technology,  
P.O. Box 513, 5300 MB Eindhoven, The Netherlands.*

(Dated: December 9, 2024)

Oblique impact of drops on a solid or liquid surface is frequently observed in nature. Most studies on drop impact and splashing, however, focus on perpendicular impact. Here, we study oblique impact onto a deep liquid pool, where we quantify the splashing threshold, maximal cavity dimensions and cavity collapse by high-speed imaging above and below the water surface. Three different impact regimes are identified: smooth deposition onto the pool, splashing in the direction of impact only, and splashing in all directions. We provide scaling arguments that delineate these regimes by accounting for drop impact angle and Weber number. The angle of the axis of the cavity created below the water surface follows the impact angle of the drop independent of the Weber number, while cavity depth and its displacement with respect to the impact position depend on the Weber number. Weber number dependency of both the cavity depth and displacement is modeled using an energy argument.

---

\* [m.v.gielen@utwente.nl](mailto:m.v.gielen@utwente.nl)

† [c.p.sleutel@utwente.nl](mailto:c.p.sleutel@utwente.nl)

‡ [h.gelderblom@utwente.nl](mailto:h.gelderblom@utwente.nl)

## I. INTRODUCTION

In nature, oblique drop impact is ubiquitous. It is for example encountered in rain drop impact [1], where it triggers air entrainment [2] and aerosol generation [3], both drive the global gas/liquid exchange. In agriculture, e.g. in pesticides crop spraying [4], oblique drop impact and the subsequent splashing and droplet rebound [5] is important. In industrial applications oblique impact occurs in e.g. metal spray deposition [6] and direct fuel injection internal combustion engines [7]. In many of these applications, splashing is an unwanted side effect after impact; it decreases deposition efficiency and may lead to widespread contamination.

While drop impact and splashing is a topic widely studied (see e.g. [8–22]), surprisingly only few papers (e.g. [23–26]) deal with non-perpendicular or oblique impact. Drop splashing upon perpendicular impact has been studied on a solid substrate [12, 13], a thin liquid film [14–16] and a deep liquid pool [17–22]. In the latter case, a cavity is formed under the water surface [2]. Collapse of this cavity [27, 28] may lead to the pinch-off of small droplets [1, 29]. These droplets emerge from a high-speed micro jet, and can reach velocities higher than the impact velocity [30]. The main parameter that governs splashing is the Weber number,  $We = \frac{\rho D U^2}{\gamma}$  with drop diameter  $D$ , drop velocity  $U$ , liquid surface tension  $\gamma$  and liquid density  $\rho$ . Also important is the Reynolds number,  $Re = \frac{UD}{\nu}$ , with  $\nu$  the kinematic viscosity. A standard splashing threshold has the form of  $We^{1/2} Re^{1/4} = K$  [8, 13] where  $K$  is a constant depending on surrounding pressure [31], on the thickness of the liquid layer and on surface roughness when impacting on a rigid substrate.

To study oblique impact, experiments on dry tilted plates [23–26] and on a moving plate [32] were performed. Bird et al. [32] showed that by moving the substrate, the velocity of the ejecta sheet and therefore the splashing threshold changes. Only a few studies [33–37] focus on oblique impact on wetted surfaces and thin liquid films. Gao and Li [37] quantify a splashing threshold for impact on a moving thin liquid film, but due to experimental complications, such as liquid inertia, this approach is not feasible for a deep liquid pool.

In numerical simulations, oblique impact on a wetted substrate [38–40] shows a transition from crown splashing to single-sided splashing. In addition, crown formation and cavity formation [40] are studied. Due to the aforementioned experimental limitations these simulations lack validation. For oblique drop impact on a wetted or dry surface, there is a clear influence of the impact angle, but to the best of our knowledge, no experiments of oblique drop impact on a liquid pool have been reported in literature until now.

Here, we present an experimental study of oblique drop impact onto a quiescent deep liquid pool. We provide details of our experimental method in section II and discuss a typical result for the impact and splashing phenomena in section III A. The angle of impact is varied systematically to quantify the splashing threshold and we present a model to explain our observations in section III B. We also quantify cavity formation and a scaling law for the cavity formation is presented in section III C.

## II. EXPERIMENTAL METHODS

To study oblique drop impact for a wide range of Weber numbers and impact angles onto a deep liquid pool, two steps are important: (i) creation of a single drop and (ii) rotation of the drop generator to obtain oblique impact. To create single drops a method previously described in [41] is used, which we adopt for oblique impact. For clarity, we briefly describe this method to isolate single drops from a stream of drops here, which is schematically drawn in Fig. 1a.

Drops are generated by pumping (Shimadzu LC-20AD HPLC pump) demineralized water (<0.1% of ammonia added for conductivity, negligible effects on surface tension) through a micropipette (Microdrop AD K-501). The continuous jet breaks up into drops by applying a piezo acoustic pressure on the jet, which transforms the jet into a stream of monodisperse drops with equal velocity. Drops of size of  $100 \pm 10 \mu\text{m}$  and velocity up to 25 m/s are generated. For these settings  $We$  ranges from 40 to 1056. This method allows for the creation of drops with a wide range of velocities and with a large enough drop spacing to prevent disturbances to the impact site due to earlier drop impact.

The drop train is directed through a ring-shaped charging electrode, where a periodic high-voltage pulse charges all passing drops except one every 10 milliseconds. Next, the drops pass another region with high electric field ( $E \geq 100$  kV/m) in between two deflection plates. The electric field separates the charged drops from the uncharged ones, and allows for the uncharged drops to continue straight and impact onto the pool. A glass container is filled to the top with water to minimize the influence of a disturbing meniscus at the container wall, which may limit the optical imaging quality. The charged drops are caught further on their path and then disposed. To create an oblique impact, the micropipette, charge electrode and deflection plates are tilted. With this method impact angles up to  $80^\circ$  from perpendicular can be obtained.

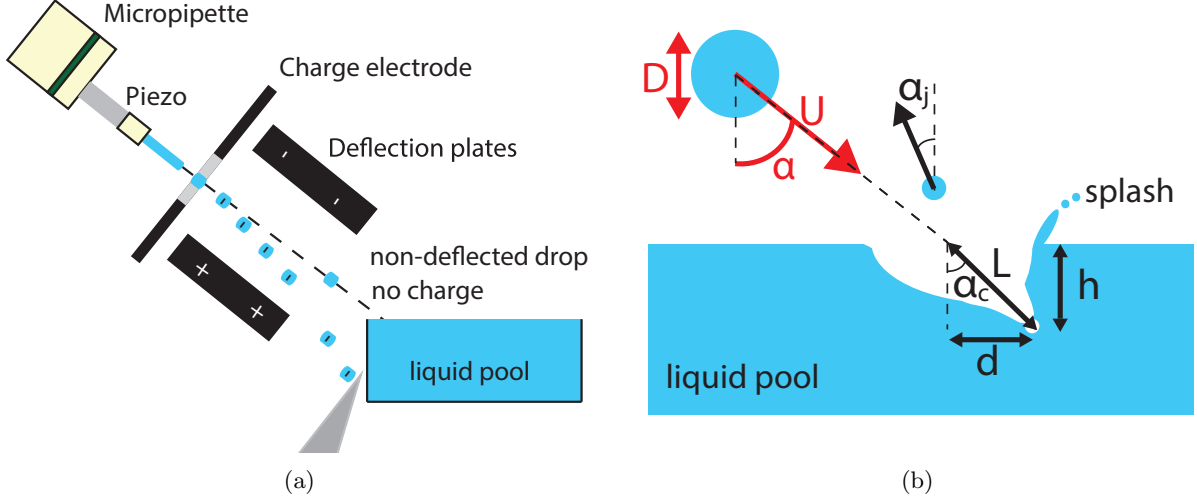


FIG. 1: a) Sketch of the experimental setup. A continuous stream of drops is created by piezoelectric-actuation of a micro jet. A charging electrode charges the drops which are subsequently deflected by the deflection plates. Every 10 milliseconds a single drop is left uncharged and can be separated from the stream. By tilting the micropipette, charging electrode and deflection plates, the impact angle  $\alpha$  of the drops onto the pool can be varied. b) Drop diameter  $D$ , velocity  $U$  and impact angle  $\alpha$  are controlled by the experiment and cavity displacement  $d$ , height  $h$  are measured, which results in cavity angle  $\alpha_c$  and the characteristic length of cavity  $L$ . Next to that, the angle of the jetted droplet out of the cavity  $\alpha_j$  is measured. The shape of the splash and the collapse of the cavity are recorded using two separate high-speed recordings above or below the water surface, respectively.

Figure 1b shows a sketch of drop velocity  $U$  and impact angle  $\alpha$ . These parameters are varied systematically, while keeping the drop diameter  $D$  constant. Drop impact is recorded in a side view using high-speed imaging (Photron SA-X2, operated at frame rates up to 100 kfps) and backlight illumination (Olympus ILP-2). From the recordings, we extract  $D$ ,  $U$  and  $\alpha$  ( $\tan\alpha = \left(\frac{U_{\parallel}}{U_{\perp}}\right)$ , where  $U_{\parallel}$  and  $U_{\perp}$  are the tangential and perpendicular component of  $U$ , respectively) using customized image-processing analysis. The impact velocity is measured from the penultimate frames just before impact to minimize the influence of air drag. We also characterize the direction of the splash and measure the angle of the jetted droplet emerging from the cavity  $\alpha_j$ .

The dynamics of the cavity is characterized simultaneously with the impact event by collecting two separate recordings for each impact condition, one above and one below the water surface, in order to compensate for the different optical focal depth. From the cavity recordings, we measure the maximum cavity displacement  $d$ , maximum height  $h$  and define the cavity angle  $\alpha_c$ , with  $\tan\alpha_c = \left(\frac{d}{h}\right)$ .

Data extracted from six combined recordings (above and below the water surface) is averaged for each impact condition. The average values allow us to relate parameters of the cavity with the impact conditions with a standard deviation of less than 5 percent. To quantify the splashing threshold above the water surface and the cavity formation and collapse below the water surface, we analyzed 1147 individual drop impacts.

### III. RESULTS AND INTERPRETATION

#### A. Typical features of oblique drop impact

Figure 2 shows the time series of a typical experiment with  $We = 674$  and  $\alpha = 28^\circ$ . Qualitatively, the different stages of impact are comparable to perpendicular impact, with some differences for oblique impact, which we will now discuss.

Panel (a) shows a snapshot 0.02 ms after the drop impacts. The formation of a hemispherical cavity has started below the water surface and an asymmetric splash ejecting small droplets is visible above the water surface. At  $t = 0.1$  ms, see panel (b), both crown and cavity are growing. In contrast to normal impact the droplets only detach on a single side. Just below the water surface, a wave crest is observed. At  $t = 0.28$  ms (panel (c)) the wave crest is highlighted with an arrow while it travels downward along the cavity wall. Here it is clearly seen that the cavity is asymmetric. At this point in time, the cavity is still growing while surface tension causes the crown to retract and the

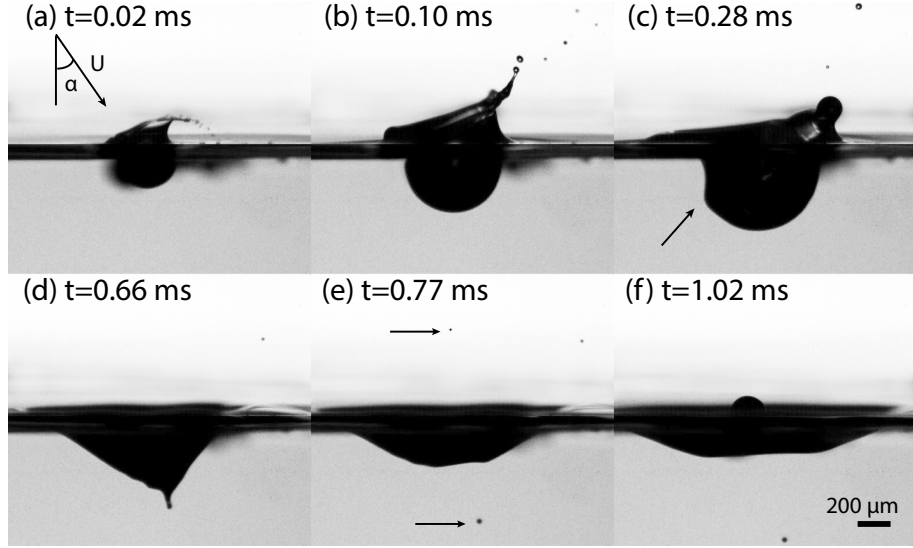


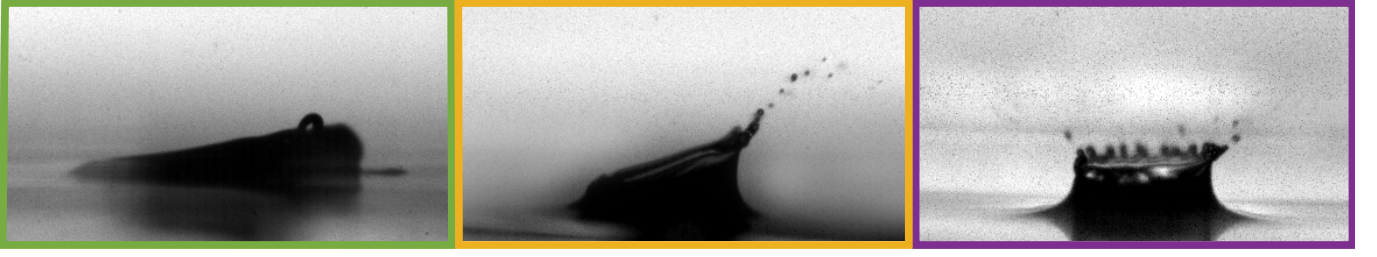
FIG. 2: Time series of a drop impacting onto the pool with a Weber number  $We = 674$  and impact angle  $\alpha = 28^\circ$ , where  $t=0$  marks the moment the drop makes first contact with the pool. Each image is composed of two independent recordings, one recording above the water to visualize the splash and the other one below the water surface to visualize the cavity, in order to compensate for the different depth of focus. Both recordings are however taken under identical experimental conditions. The images were then combined to show the entire impact process in a single time series. (a) The impacting drop causes a splash that fragments into droplets. Here, the splash is formed on a single side only. (b) A crown develops and remains more pronounced on one side. The cavity has a hemispherical form and is growing. (c) The splashing is finished and the cavity still grows. An arrow points to the wave crest, which travels downwards along the cavity surface, see [28]. The oblique impact leads to an asymmetry of the cavity. (d) The capillary wave focuses off-center at the bottom of the cavity. (e) Collapse of the wave leads to the entrainment of a bubble and retraction of the jet leads to the ejection of tiny droplets during closure of the cavity. The arrows indicate the position of the entrained bubble and the droplets. (f) A Worthington jet is formed during closure of the cavity.

rim to grow thicker. Panel (d) ( $t = 0.66\text{ms}$ ) shows the cavity at its deepest point, where the maximal cavity depth and displacement are reached. Now, the closure of the cavity starts and the capillary wave crest collides at the bottom of the cavity. During the collision of these waves, an air bubble can be entrapped [2]. The tip at the bottom of the cavity in (d) marks this air bubble just before pinch-off. The tip will retract quickly due to the high local curvature. The series of subsequent image frames suggest that the jetted droplet which is visible above water in panel (e) at  $t = 0.77\text{ ms}$ , originates from the rapid tip retraction. The droplets jetted out of the cavity reach velocities of the same order as the main drop impact velocity. Below the water (panel (e)) a tiny bubble is clearly visible. At  $t = 1.02\text{ ms}$  (panel (f)) the cavity is completely collapsed, marked by the emergence of a thick Worthington jet [42].

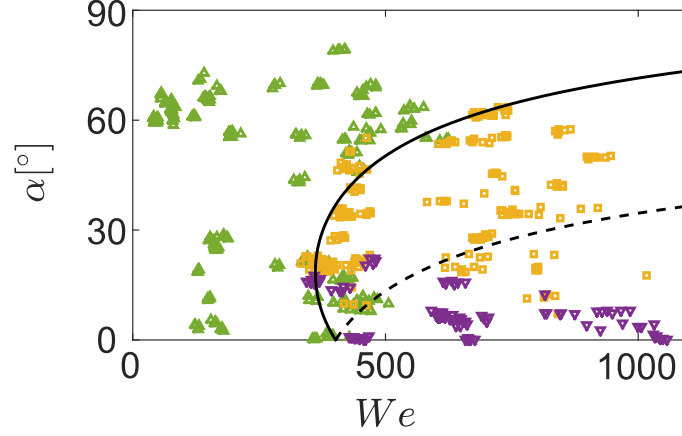
### B. Splashing threshold

After drop impact three different phenomena can be observed above the water surface, as illustrated in Fig. 3a. First, the drop can smoothly coalesce with the liquid pool. This behavior is identified as deposition. Secondly, a crown can be formed which destabilizes on a single side of the drop, resulting in the ejection of satellite droplets at the tips of the crown on this side of the drop. The direction of splashing corresponds to the direction of impact. This behavior is denoted as single-sided splashing. The final phenomenon observed is the ejection of small satellite droplets from the crown in all directions, which is indicated as omni-directional splashing. We quantify these phenomena in a phase diagram of  $\alpha$  and  $We$  illustrated by three distinct regions, see Fig. 3b. For a single value of  $\alpha$  the impact behavior can change from deposition to single-sided splashing to omni-directional splashing by increasing  $We$ . Similarly, for a single value of  $We$  the impact behavior can change from omni-directional splashing to single-sided splashing to deposition for increasing  $\alpha$ .

We now provide a scaling argument to explain these observations. To find the splashing threshold for oblique impact, we aim to describe the velocity of the crown in terms of  $U$ ,  $D$ ,  $\alpha$  and  $We$ . We start by considering perpendicular (i.e.



(a)



(b)

FIG. 3: a) Three types of impact behavior are observed above the water surface. From left to right: deposition (green), single-sided splashing (yellow) and omni-directional splashing (purple). b) A phase diagram of the impact behavior as a function of  $We$  and impact angle  $\alpha$ . The color codes correspond to Fig. a): upward green triangles represent deposition, yellow squares represent single-sided splashing and downward purple triangles represent omni-directional splashing. The solid and the dashed line are derived from Eqn. (4) with  $c = 0.33$ , where the solid line represents the splashing threshold from deposition to single-sided splashing (Eqn. (4) with minus sign) and the dashed line indicates the splashing threshold from single-sided splashing to omni-directional splashing (Eqn. (4) with plus sign).

vertical) impact. A schematic view of the drop during splashing is shown in Fig. 4a. In this case, the flow into the crown is distributed symmetrically. Once the entire drop has impacted, we can assume that the entire drop volume is proportional to the volume of the crown, which gives (per unit time)

$$D^2U \sim eDV, \quad (1)$$

where  $e$  is the thickness of the crown at its origin. In line with a model for splashing of the fast ejecta on a thin liquid film [15], we assume that in order to obtain splashing upon impact on a liquid pool the velocity of the crown  $V$  has to be larger than the Taylor Culick velocity  $V_{TC} \sim \sqrt{\frac{\gamma}{\rho e}}$ . Thoroddsen [21] showed experimentally that  $e \sim \sqrt{\nu t}$ , consistent with dimensional analysis. Using  $t \sim \frac{D}{V}$  in the expression for  $e$  and (1) to express  $V$  we find the splashing criterion

$$\frac{V}{V_{TC}} \sim We^{1/2} Re^{1/4} > K, \quad (2)$$

where  $K$  is the critical number for splashing [8, 9, 43]. The numerical value of  $K$  depends on specific experimental conditions, such as the flow profile inside the crown [15]. Previous studies reported  $K \approx 54$  for a rigid surface [9],  $K \approx 160$  for a thin liquid film [14] and  $K \approx 90$  for a deep liquid pool [20]. For our experiments we determine for perpendicular impact ( $\alpha \simeq 0^\circ$ ) a critical Weber number for splashing of about  $We_s \approx 400$  which leads to  $K \approx 130$ .

For oblique impact the mass is no longer symmetrically distributed over the crown: the mass flow into the crown increases on one side of the drop and decreases on the other side of the drop (Fig. 4b). This unequal mass distribution

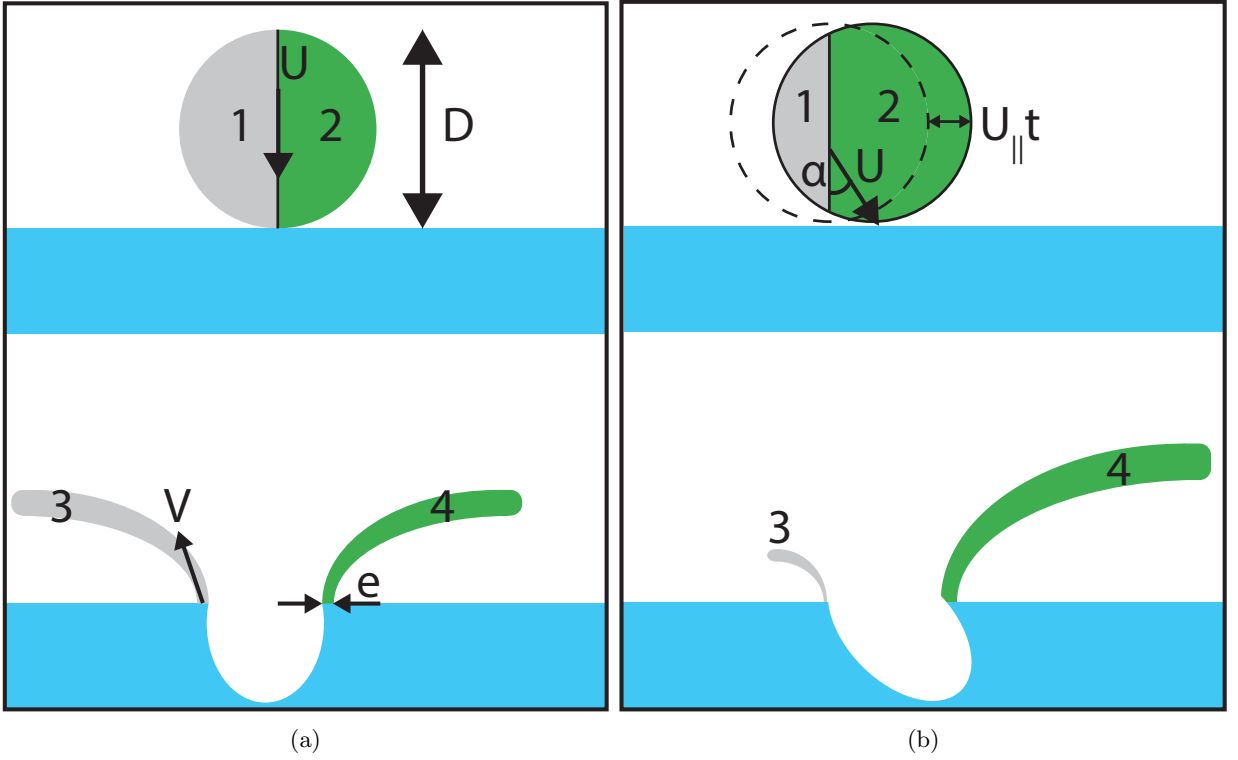


FIG. 4: Schematic illustration of the mass distribution in the crown. Volume 1 indicates the part of the original drop that flows into crown volume 3. Volume 2 represents the part of the original drop that flows into crown volume 4. Volume 1 and 3, and 2 and 4 are identical due to mass conservation. a) For normal drop impact the volume of the original drop is distributed evenly over the crown, such that volume 1 and 2, and thus 3 and 4 are identical. b) For oblique impact,  $U_{\parallel}$  will cause a shift (solid line) in drop position with respect to the normal impact (dashed line). This shift reduces volume 1 and increases volume 2 by an amount of  $\pm \rho D U_{\perp} U_{\parallel} t$  (see text). As a result, the crown becomes asymmetrical.

originates from the contribution of the tangential component of the impact velocity  $U_{\parallel} = U \cdot \sin \alpha$ . On one side of the drop,  $U_{\parallel}$  leads to an increased mass flow, while on the other side the mass flow is decreased. The added/reduced mass flow rate into the crown scales as  $\pm \rho D U_{\perp} U_{\parallel} t$  respectively, where  $U_{\perp} = U \cdot \cos \alpha$  sets the speed with which the drop is moving down into the pool.

To account for this additional mass flow, we can rewrite (1) as

$$D^2 U_{\perp} \pm D U_{\perp} U_{\parallel} t \sim e D V. \quad (3)$$

The (critical) velocity for crown splashing now depends both on  $U_{\perp}$  and  $U_{\parallel}$ . From (3) it follows that  $U_{\perp} \left[ 1 \pm \frac{U_{\parallel} t}{D} \right] \sim \frac{V e}{D}$ . We observe in experiment that splashing starts at the same time scale as the drop fully impacts the liquid pool  $t \sim c \frac{D}{U_{\perp}}$ , which leads to a splashing threshold:

$$\frac{V}{V_{TC}} \sim W e^{1/2} R e^{1/4} \frac{(\cos \alpha_s)^{5/4}}{c^{1/4}} [1 \pm c \tan \alpha_s] > K, \quad (4)$$

where  $c$  is a fitting parameter. In (4), we use  $K = 130$  (as determined for perpendicular impact) to find the splashing threshold as a function of  $W e$  and  $\alpha_s$ . These considerations suggest that there are two transitions in the phase space of Fig 3b: (i) the solid line defines where  $V_{TC}$  is reached on a single side of the drop, which indicates the transition from deposition to single-sided splashing. (ii) The dashed line defines where  $V_{TC}$  is reached for splashing in all directions, which indicates the transition from single-sided splashing to omni-directional splashing. In Fig. 3b we plot these transitions and we find good agreement with the experimental data using  $c \approx 0.33$ .

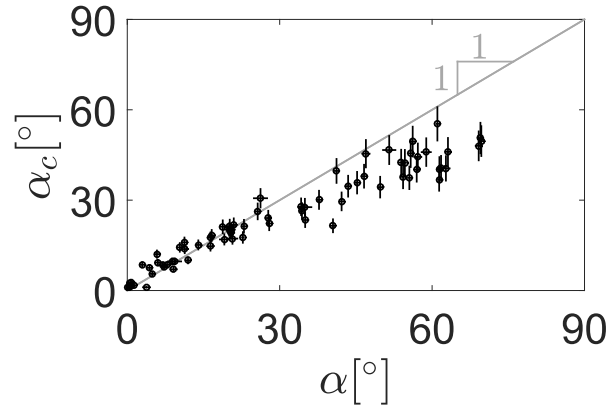


FIG. 5: Cavity angle  $\alpha_c$  as a function of the impact angle  $\alpha$ . The solid line has slope of unity. For increasing  $\alpha$  the distinctness of  $d$  and  $h$  decreases. Therefore, the error in measuring  $\alpha_c$  increases with  $\alpha$  and is estimated to be 10% of  $\alpha$ .

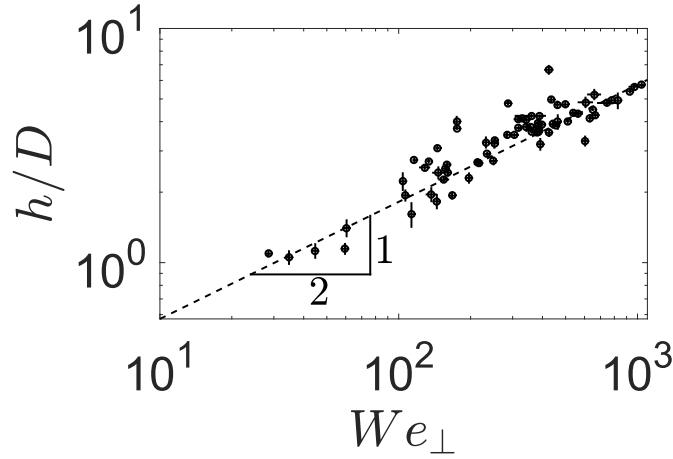


FIG. 6: Double logarithmic plot of the maximum cavity depth  $h$  as a function of the Weber number, based on the normal impact velocity  $We_{\perp}$ . The dashed line corresponds to Eqn. (6) with slope 1/2 and a prefactor of 0.18.

### C. Cavity formation

From our recordings we extract the angle  $\alpha_c$  (as defined in fig 1b) and the dimensions of the cavity ( $h$  and  $d$ ). In Fig. 5 the cavity angle  $\alpha_c$  is plotted as a function of impact angle  $\alpha$ . For small impact angles  $\alpha_c$  equals the impact angle. This is expected since the momentum of the drop is transferred to the cavity in the direction of impact. However, for impact angles larger than  $\alpha \gtrsim 30^\circ$ ,  $\alpha_c$  gets increasingly smaller as compared to  $\alpha$ . The measurement error of  $\alpha_c$  is estimated to be 10 % of  $\alpha$ ; however, this does not explain the observed decrease. A possible explanation for the deviation in proportionality of  $\alpha_c$  with  $\alpha$  for larger impact angles could come from additional wave drag [44] for drops moving close to parallel to the surface (i.e. large  $\alpha$ ). Due to the build-up of waves in the direction tangential to the surface, part of the energy can be dissipated into those waves for larger impact angles which leads to a smaller increase in cavity angle. We also analyzed the cavity angle as a function of  $We$ , but no significant dependency was found (data not shown).

We now present data on the maximum cavity depth and maximum displacement. The maximum cavity depth  $h$  and displacement  $d$  is plotted in Fig. 6 and Fig. 7 as a function of  $We$  based on the normal impact velocity  $We_{\perp} = \frac{\rho D U_{\perp}^2}{\gamma}$  and the tangential velocity  $We_{\parallel} = \frac{\rho D U_{\parallel}^2}{\gamma}$ , respectively. We observe that  $h$  scales with  $We_{\perp}^{1/2}$  while  $d$  scales with  $We_{\parallel}^{1/2}$ .

The observed scaling can be explained from energy conservation. We consider that the kinetic energy of the



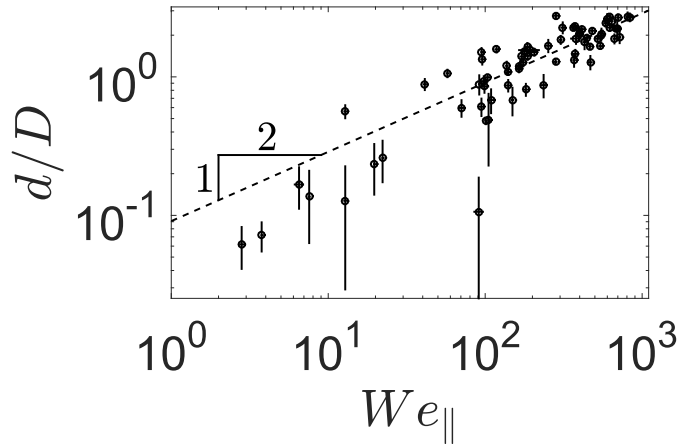


FIG. 7: Double logarithmic plot of the maximum horizontal cavity displacement  $d$  as a function of the Weber number based on the tangential impact velocity  $We_{\parallel}$ . The dashed line corresponds to Eqn. (7) with slope 1/2 and a factor of 0.09.

impacting drop is proportional to the additional surface energy to create the cavity, given by

$$\rho D^3 U^2 \sim \gamma L^2, \quad (5)$$

where  $L$  is the characteristic length of the cavity, as shown in Fig. 1b. For oblique impact experiments,  $L$  depends on both  $h$  and  $d$  since the maximum depth of the cavity is displaced by  $d$  as a consequence of the tangential component of the impact velocity, resulting in  $L \sim \sqrt{h^2 + d^2} \sim h\sqrt{1 + \tan^2 \alpha}$ . Here we have assumed  $\tan \alpha = \frac{d}{h}$ , which will introduce a small error for  $\alpha \gtrsim 30^\circ$ , as seen in Fig. 5.

From (5) we find  $\frac{L}{D} \sim We^{1/2}$ . Using the geometrical relation for  $L$  leads to  $\frac{h}{D} \sim We^{1/2} \cos \alpha$ , and hence

$$\frac{h}{D} \sim We_{\perp}^{1/2}. \quad (6)$$

Fig. 6 shows (6) together with the experimentally determined maximum cavity depth, where we used a prefactor of 0.18. For the maximum cavity displacement we find  $\frac{d}{D} \sim \frac{h}{D} \tan \alpha \sim We^{1/2} \sin \alpha$ , which gives

$$\frac{d}{D} \sim We_{\parallel}^{1/2}. \quad (7)$$

We plot in Fig. 7 the experimentally determined maximum cavity displacement with slope 1/2 and a prefactor of 0.09 which provided the best fit to the experimental data.

#### IV. DISCUSSION ON CAVITY COLLAPSE

The collapse of a cavity is sometimes accompanied by the jetting of a droplet out of the cavity. In this subsection we aim to quantify the direction of the jetting behavior. Figure 1b depicts the angle  $\alpha_j$  at which the droplet is jetted out of the cavity. Not every impact leads to the observation of a jetted droplet, which could mean that no droplets were pinched off from the jet, or that droplets remain trapped inside the cavity. Given the small droplet size and the limited depth of field of our imaging system, the ejected droplet could also have moved out of the optical focal plane.

Another observation is that the trajectory of the droplet is curved when it moves out of the cavity, as shown in Fig. 8a. This may be an indication that the initial  $\alpha_j$ , directly after pinch-off from the jet, is different from the  $\alpha_j$  measured above the closing cavity, where it may be hindered by a disturbing airflow. To better quantify the jet direction, we change our focus to the cavity collapse and deduce the retraction angle  $\alpha_r$ , as depicted in Fig. 8b, where we assume that the onset of retraction of the cavity sets the initial direction of the jetted drop. From a series of frames  $\alpha_r$  is measured where the first frame was taken when the cavity is at its maximum size. In the next frames we follow the direction of cavity collapse by tracking this point to give the retraction angle.

As shown in Fig. 9a,  $\alpha_j$  and  $\alpha_r$  are indeed similar. Over the entire range,  $\alpha_j$  is slightly smaller than  $\alpha_r$ , which is probably due to the influence of a disturbing airflow, as discussed above.  $\alpha_r$  follows  $\alpha$  up to about  $25^\circ$ . For  $\alpha >$



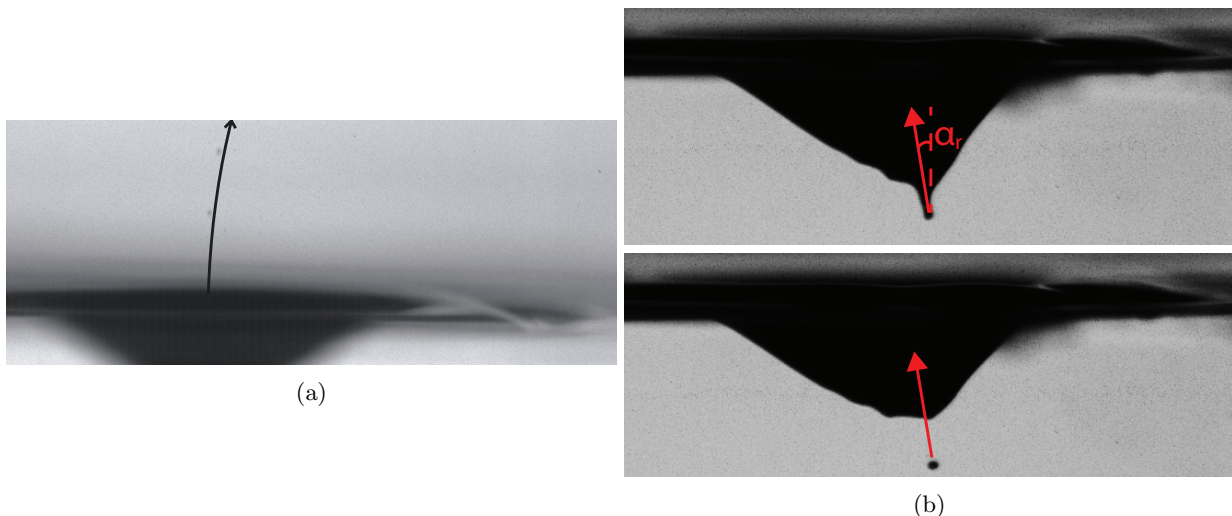


FIG. 8: a) The trajectory of two jetted droplets for  $We = 371$  and  $\alpha = 0.3^\circ$  shows a deflection when the droplets leave the cavity. This deflection is indicated by the arrow. b) Snapshot of the cavity at its maximal dimensions (top), and snapshot of the cavity approximately 14 microseconds later (bottom), where the collapse and tip retraction have started. The red arrows indicate the direction in which the cavity starts to collapse, used as a measure for the direction of the jetted droplet out of the cavity.

$25^\circ$ ,  $\alpha_r$  flattens and reaches a maximum of  $30^\circ$ . The deviation from  $\alpha$  occurs around the same  $\alpha$  for both  $\alpha_c$  and  $\alpha_r$ . However, the build-up of drag waves in front of the impacting drop is not enough to account for the flattening observed for  $\alpha_r$ . We speculate that this saturation is caused by a maximum angle that the cavity can make with the surface. For perpendicular impact, the cavity is symmetric and hemispherical, which is energetically most favorable. For oblique impact, the cavity is no longer hemispherical but one side of the cavity wall starts to move inwards (see fig 9b). At the other side the cavity opening grows due to surface tension. The sharp edge rapidly retracts by surface tension, much more than at the opposite side of the cavity which is shown in Fig. 9b by the hatched area. This effect breaks the symmetry and therefore poses a limit on the maximum value of  $\alpha_r$ .

## V. DISCUSSION AND CONCLUSIONS

We present an experimental study of oblique drop impact onto a quiescent deep liquid pool. We performed quantitative experiments where oblique drops impact onto a deep liquid pool for a wide range of  $We$  and impact angles  $\alpha$  and analyzed the splashing behavior, the cavity formation and the cavity collapse.

In analogy to previous studies e.g. [8, 9, 15, 43], we found that the crown velocity has to be larger than the Taylor-Culick velocity to obtain splashing. For oblique drop impact this crown velocity is influenced by the tangential velocity of the impacting drop, leading to an asymmetry in the crown and giving rise to an asymmetry in the splashing threshold [32]. In contrast to the model presented in [32] where oblique drop impact on a dry substrate was studied, we cannot describe our data by simply adding/subtracting the tangential velocity to the crown velocity. Instead, we assume the tangential velocity influences the amount of mass squeezed into the crown. We quantify this effect using scaling arguments and derived a model that is consistent with our measurements for a wide range of  $We$  and  $\alpha$ . Thus, the model gives valuable insight into splashing occurrence and direction.

For small impact angle  $\alpha$  the cavity angle directly equals the impact angle and does not depend on  $We$ , for large  $\alpha$  a decrease in  $\alpha_c$  with respect to  $\alpha$  was observed. The magnitude of the cavity displacement depends on the tangential Weber number and the cavity depth depends on the perpendicular Weber number. The scarce numerical simulations on oblique impact [40] confirm this  $We$ -dependence of the cavity displacement. However, since [40] described drop impact on a thin liquid film, no information on the cavity depth is available.

In conclusion, our study provides the first quantitative overview of the events following oblique impact onto a deep quiescent liquid pool. The results allow to predict under what impact velocity and in what direction drops can splash after impact. In our experiment, data from a single measurement plane is obtained. It would be interesting to obtain the full 3D profile above and below the water surface using holographic microscopy [45] or by extended numerical simulations.

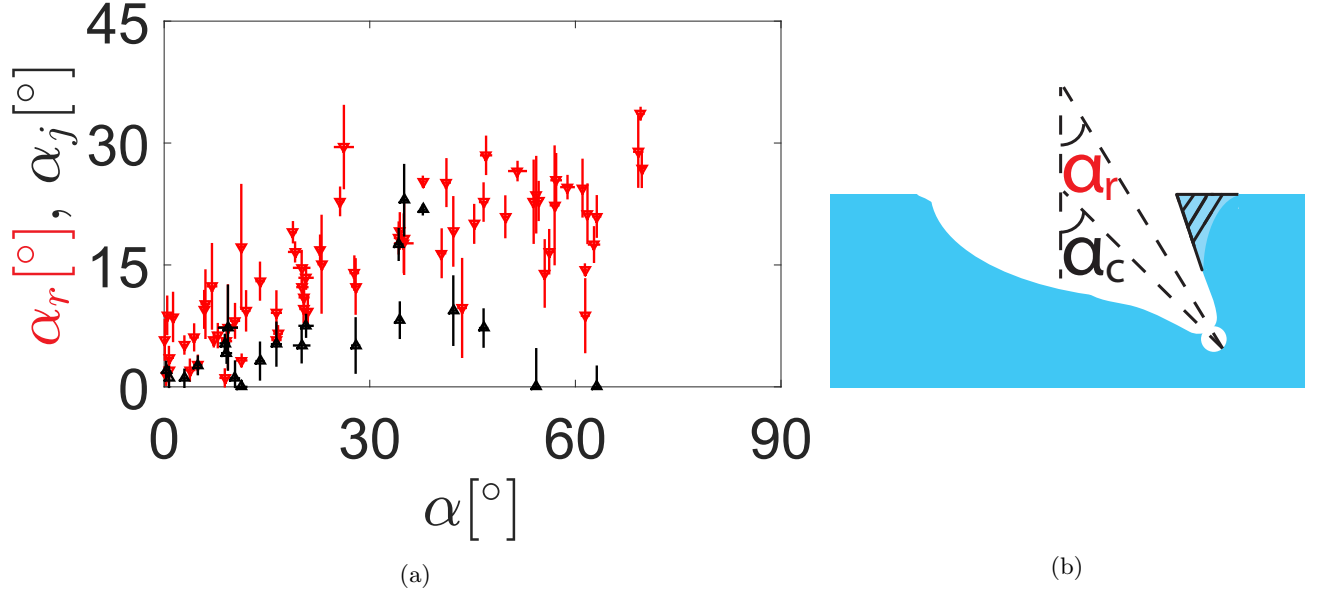


FIG. 9: (a) Angle of the droplet jetted out of the cavity  $\alpha_j$  (upward black triangles, each triangle corresponds to a single measurement) and retraction angle of the cavity  $\alpha_r$  (downward red triangles, each triangle corresponds to the average taken over six measurements below and above the water surface) as a function of the impact angle  $\alpha$ . (b) Schematic view of the cavity angle and the retraction angle. When a drop impacts obliquely, one expects a cavity consisting of the white area, due to symmetry. However, since surface tension prohibits the existence of the sharp corner, the hatched area is pulled outward. Therefore, an asymmetric cavity forms resulting in a retraction angle which is smaller compared to the cavity angle.

### ACKNOWLEDGMENTS

We acknowledge the Industrial Partnership Programme of the Foundation for Fundamental Research on Matter (FOM), which is financially supported by the Netherlands Organization for Scientific Research (NWO), and NanoNextNL, a micro and nanotechnology consortium of the Government of the Netherlands and 130 partners. We also acknowledge C.W. Visser for support during experiments and K. Winkels, J.F. Dijksman and B. de Smet for stimulating discussions.

MVG and PS contributed equally to this work.

- 
- [1] M. Rein, *Journal of Fluid Mechanics* **306**, 145 (1996).
  - [2] H. N. Oguz and A. Prosperetti, *Journal of Fluid Mechanics* **219**, 143 (1990).
  - [3] K. Sellegri, C. O'Dowd, Y. Yoon, S. Jennings, and G. de Leeuw, *Journal of Geophysical Research Atmospheres* **111** (2006), 10.1029/2005JD006658.
  - [4] C. Peirce, C. Priest, T. McBeath, and M. McLaughlin, *Soft Matter* **12**, 209 (2016).
  - [5] T. Gilet and J. W. M. Bush, *Physics of Fluids* **24** (2012).
  - [6] Z. Djuric and P. Grant, *Modelling and Simulation in Materials Science and Engineering* **9**, 111 (2001).
  - [7] Z. Wang, H. Du, J. Liu, L. Han, and S. Liu, *Advanced Materials Research* **347-353**, 770 (2012).
  - [8] C. Mundo, M. Sommerfeld, and C. Tropea, *International Journal of Multiphase Flow* **21**, 151 (1995).
  - [9] C. Josserand and S. Thoroddsen, *Annual Review of Fluid Mechanics* **48**, 365 (2016).
  - [10] S. Thoroddsen, K. Takehara, and T. Etoh, *Journal of Fluid Mechanics* **706**, 560 (2012).
  - [11] L. Zhang, J. Toole, K. Fezzaa, and R. Deegan, *Journal of Fluid Mechanics* **703**, 402 (2012).
  - [12] A. L. Yarin and D. A. Weiss, *Journal of Fluid Mechanics* **283**, 141 (1995).
  - [13] A. Yarin, *Annual Review of Fluid Mechanics* **38**, 159 (2006).
  - [14] R. D. Deegan, P. Brunet, and J. Eggers, *Nonlinearity* **21**, C1 (2008).
  - [15] C. Josserand and S. Zaleski, *Physics of Fluids* **15**, 1650 (2003).
  - [16] I. V. Roisman and C. Tropea, *Journal of Fluid Mechanics* **472**, 373 (2002).
  - [17] J. O. Marston and S. T. Thoroddsen, *Journal of Fluid Mechanics* **614**, 293 (2008).

- [18] B. Ray, G. Biswas, and A. Sharma, *Physics of Fluids* **24**, 082108 (2012).
- [19] B. Ray, G. Biswas, and A. Sharma, *Journal of Fluid Mechanics* **768**, 492 (2015).
- [20] E. Castillo-Orozco, A. Davanlou, P. K. Choudhury, and R. Kumar, *Phys. Rev. E* **92**, 053022 (2015).
- [21] S. T. Thoroddsen, *Journal of Fluid Mechanics* **451**, 373 (2002).
- [22] T. Tran, H. De Maleprade, C. Sun, and D. Lohse, *Journal of Fluid Mechanics* **726**, R3 (2013).
- [23] Š. Šikalo and E. Ganić, *Experimental Thermal and Fluid Science* **31**, 97 (2006).
- [24] Š. Šikalo, C. Tropea, and E. Ganić, *Journal of Colloid and Interface Science* **286**, 661 (2005).
- [25] C. Antonini, F. Villa, and M. Marengo, *Experiments in Fluids* **55**, 1 (2014).
- [26] D. G. K. Aboud and A.-M. Kietzig, *Langmuir* **31**, 10100 (2015).
- [27] R. Bergmann, D. van der Meer, S. Gekle, A. van der Bos, and D. Lohse, *Journal of Fluid Mechanics* **633**, 381 (2009).
- [28] S. Gekle, A. Van Der Bos, R. Bergmann, D. Van Der Meer, and D. Lohse, *Physical Review Letters* **100** (2008).
- [29] S. Gekle, J. Gordillo, D. Van Der Meer, and D. Lohse, *Physical Review Letters* **102** (2009).
- [30] M. Longuet-Higgins and H. Oguz, *Journal of Fluid Mechanics* **290**, 183 (1995).
- [31] L. Xu, W. W. Zhang, and S. R. Nagel, *Phys. Rev. Lett.* **94**, 184505 (2005).
- [32] J. C. Bird, S. S. H. Tsai, and H. A. Stone, *New Journal of Physics* **11**, 063017 (2009).
- [33] S. K. Alghoul, C. N. Eastwick, and D. B. Hann, *Experiments in Fluids* **50**, 1305 (2011).
- [34] T. Okawa, T. Shiraishi, and T. Mori, *Experiments in Fluids* **44**, 331 (2008).
- [35] Z. Che, A. Deygas, and O. K. Matar, *Phys. Rev. E* **92**, 023032 (2015).
- [36] G. Liang, Y. Guo, Y. Yang, N. Zhen, and S. Shen, *Acta Mechanica* **224**, 2993 (2013).
- [37] X. Gao and R. Li, *Phys. Rev. E* **92**, 053005 (2015).
- [38] M. Cheng and J. Lou, *Computers and Fluids* **115**, 11 (2015).
- [39] P. Brambilla and A. Guardone, *Computing* **95**, 415 (2013).
- [40] B. Ray, G. Biswas, and A. Sharma, *Communications in Computational Physics* **11**, 1386 (2012).
- [41] C. W. Visser, P. E. Frommhold, S. Wildeman, R. Mettin, D. Lohse, and C. Sun, *Soft Matter* **11**, 1708 (2015).
- [42] A. Worthington, *A study of splashes* (Longmans, Green, and Co., 1908).
- [43] C. D. Stow and M. G. Hadfield, *Proceedings of the Royal Society of London A: Mathematical, Physical and Engineering Sciences* **373**, 419 (1981).
- [44] M. Le Merrer, C. Clanet, D. Quéré, E. Raphaël, and F. Chevy, *Proceedings of the National Academy of Sciences* **108**, 15064 (2011).
- [45] U. Schnars and W. Jüptner, *Measurement Science and Technology* **13**, R85 (2002).